ACS Photonics

pubs.acs.org/journal/apchd5 Article

Subwavelength, Phase-Sensitive Microscopy of Third-Order Nonlinearity in Terahertz Frequencies

Tong Lin, Rui Xu, Xiaotong Chen, Yuxuan Guan, Mingxing Yao, Junhao Zhang, Xinwei Li, and Hanyu Zhu*

Cite This: *ACS Photonics* 2024, 11, 33−41 **Read Online**

ACCESS | Metrics & More | Article Recommendations | Supporting Information

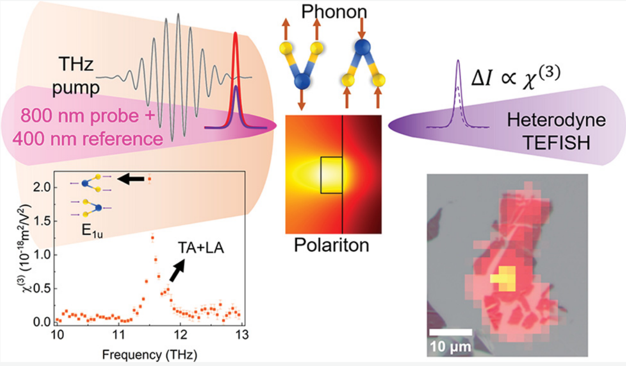

ABSTRACT: The third-order nonlinear susceptibility $\chi^{(3)}$ occurs universally in materials and can provide label-free fingerprints of materials' electronic, vibrational, and structural information. One quantitative spectroscopic method to access low-energy resonances of $\chi^{(3)}$ is the terahertz electric-field-induced second harmonic generation (TEFISH), which is particularly suitable for centrosymmetric materials without second-order processes. However, using TEFISH to measure the $\chi^{(3)}$ spectra requires light sources with high spectral intensity between 5 and 15 THz and is more challenging precisely because of the phonon bands in many materials. Here, for the first time, we report phase-sensitive heterodyne TEFISH microscopy offering simultaneous temporal, spectral, and spatial resolution, incorporating an intense and frequency-tunable narrowband terahertz source by chirped pulse difference frequency generation in the frequency range of 4−18 THz. We demonstrated time-resolved hyperspectral TEFISH microscopy in polymer thin films (SU-8), 2D crystalline semiconductors (MoS_2), and subwavelength photonic resonators. By interfering with the nonlinear emission with a local oscillator field, we quantitatively retrieved the frequency, amplitude, and relative phase of the $\chi^{(3)}$ spectra. TEFISH microscopy allows time-resolved imaging of vibrational and photonic resonances with subwavelength resolution and higher sensitivity compared to linear Fourier transform infrared spectroscopy, as well as versatility for samples in different environments by avoiding near-field probes.

KEYWORDS: *subwavelength imaging, terahertz spectroscopy, nonlinear optics, nanophotonics, heterodyne detection*

■ INTRODUCTION

Nonlinear optical hyperpolarizability is an important property that reveals the presence of electronic, vibrational, and photonic excitations and resonances in materials. Significant efforts have been made on developing spectroscopic methods for observing the third-order nonlinear susceptibility $\chi^{(3)}$, which is allowed in any material without any requirement for crystalline symmetry. For example, vibrational resonance-enhanced $\chi^{(3)}$ enables time-resolved infrared spectroscopy, coherent anti-Stokes Raman spectroscopy (CARS), and stimulated Raman scattering for applications such as imaging molecules in unlabeled cells, but these methods are usually qualitative rather than quantitative about the magnitude of $\chi^{(3)}$ nonlinearity.[1−3] The low-energy (mid- to far-infrared) resonance may be quantitatively measured with high spectral resolution by optical hyper-Raman spectroscopy, which relies on higher-order $\chi^{(5)}$ processes and often applies to either bulk materials or metallic surface-enhanced adsorbates.[4] A few existing methods can quantitatively measure $\chi^{(3)}$, like Z-scan,[5] electric-field-induced second-harmonic generation (EFISH),[6−8] and Hyper-Rayleigh scattering.[9,10] However, they are difficult to implement in the so-called "new terahertz (THz) gap", i.e., the frequency range of 5−15 THz, due to the limited access to high-field sources.[11,12] This frequency range is associated with intriguing phenomena in quantum materials such as structural control, magnetic order switching, and photoinduced superconductivity.[13−20] Recent progress in THz optics has enabled rich nonlinear spectroscopy and imaging techniques based on bright tabletop sources in this frequency range.[21−29] Quantitative THz EFISH (TEFISH) will allow the direct observation of hyperpolarization, atomic displacement, and phase transition in quantum materials.[30−34] Yet to date, TEFISH with both amplitude and phase information can only be performed for crystals without centrosymmetry, whose

Received: June 9, 2023
Revised: October 26, 2023
Accepted: October 26, 2023
Published: November 15, 2023

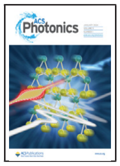

https://doi.org/10.1021/acsphotonics.3c00787
ACS Photonics 2024, 11, 33−41

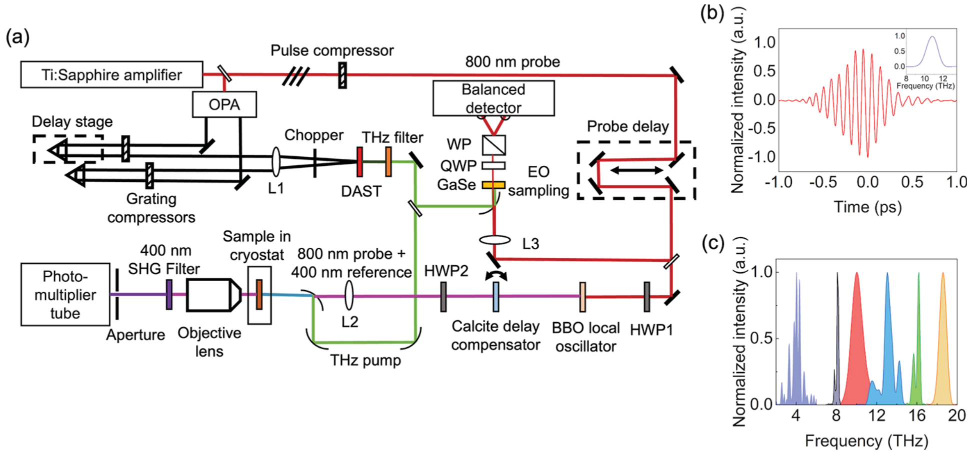

Figure 1. Schematics of the experimental setup. (a) The narrowband THz pulse is generated by chirped pulse DFG in DAST. The bandwidth of the THz pulse is tunable by adjusting the chirp of NIR pulses. Heterodyne TEFISH spectroscopy is achieved by introducing a local oscillator field generated by beta barium borate which is much stronger than the TEFISH field. Thus, the measured signal is linearly proportional to $\chi^{(3)}$. The output signal is collected by an objective (NA = 0.28), filtered, and detected by a photomultiplier tube. L1, L2, L3 − lens, BS − beam splitter, WP − Wollaston prism, QWP − quarter-wave plate, and HWP − half-wave plate. (b) The electric field of the THz pulse and spectral intensity (inset) detected by electric-optic sampling. The pulse is 350 fs long and centered at 11 THz with a bandwidth of 1 THz. (c) Frequency tunability of the THz pulse. The center frequency of the THz pulse is tunable in the range 4−18 THz by adjusting the relative delay and wavelengths of the NIR pulses.

second harmonic generation (SHG) serves as a local oscillator (LO).[35]

Here, we report TEFISH microscopy to quantitatively probe $\chi^{(3)}$ in centrosymmetric materials with spatial and temporal resolution. The spectral range of the light source is from 4 to 18 THz. We generated the LO field by an external nonlinear crystal that interferes with the TEFISH field to determine both the amplitude and phase. Since the heterodyne signal scales linearly with the sample volume, as opposed to the signal from intensity-only measurements with quadratic scaling, the former decreases slower with decreasing volume than the latter, and thus, the sensitivity for heterodyne detection is higher for small samples. The sensitivity can be further improved with stronger THz drive fields, whose fluence is negligible compared with the probe pulses and thus is not a limiting factor regarding sample damage. To prove the concept, we performed phase-sensitive TEFISH to reveal the spectral fingerprint of $\chi^{(3)}$ from infrared-active phonons of two-dimensional semiconductor MoS_2, as well as the enhanced THz field in subwavelength surface phonon polariton (SPhP) resonators based on ionic crystal CaF_2. The time-resolved TEFISH signal not only provides information about the resonance frequency and line shape but also visualizes the atomic displacement of the excited coherent phonons. The $\chi^{(3)}$ spectra obtained from TEFISH measurement resemble those from linear infrared spectroscopy according to Miller's rule $\chi^{(3)}(2\omega \pm \Omega; \omega, \omega, \Omega) \propto \chi(2\omega \pm \Omega)\chi(\omega)^2 \chi(\Omega)$, where Ω and ω are the frequencies of the THz excitation and the optical probe, respectively, and χ is the linear susceptibility. Meanwhile, TEFISH as a coherent technique gains extra access to the entire $\chi^{(3)}$ tensor determined by the selection rule. It also takes advantage of the high spatial resolution and double enhancement from both the phonon resonance with the THz pump and the electronic resonance with the optical probe and thus is potentially more sensitive than Fourier transform infrared spectroscopy, which only exploits vibrational resonance. The sub-diffraction-limited imaging with respect to the THz wavelengths is achieved via nonlinear conversion to signals in the visible wavelength by far-field probes and hence may be more versatile than near-field probes for samples in cryogenic or high temperatures, reactive environments, or buried deep beneath the surface. The simultaneous temporal, spectral, and spatial resolution of third-order nonlinearity in the THz domain potentially offers a new powerful approach for studying phononic, magnetic, and organic materials.

Experimental Setup. To acquire time-domain phase-sensitive TEFISH with better spatial resolution, we developed a heterodyne TEFISH system that combines three key features: the THz source, a collinear interferometer, and a confocal microscope. First, intense narrowband source is less accessible for the range of 5−15 THz because of the conventional nonlinear crystals' own phonon absorption resonance.[11,12,21,36] Recent development of novel organic nonlinear crystals has enabled the possibility of intense THz radiation generation in the frequency range of 5−15 THz due to their large nonlinear optical susceptibilities and great phase-matching condition.[37] Among them, 4-*N*,*N*-dimethylamino-4′-*N*′-methyl-stilbazolium tosylate (DAST) is one of the most widely investigated crystals because it shows efficient difference frequency generation (DFG) in the THz regime.[38] To produce intense narrowband pulses in the mid- to far-infrared frequencies, we adopted a scheme of chirped pulse DFG from the broadband near-infrared (NIR) output of typical table-top optical parametric amplifiers (OPAs).[21−23,25] Second, typical TEFISH is an inherent homodyne detection method for centrosymmetric materials whose $\chi^{(2)}$ is zero, meaning that phase information is lost during the measurement. Moreover, the output signal scales quadratically with the TEFISH field and appears at twice the real frequency, which can cause ambiguities in its physical interpretation.[32,33] Previously, phase-sensitive heterodyne measurements of other nonlinear processes such as two-dimensional femtosecond spectroscopy and heterodyne sum frequency generation spectroscopy were realized by interfering the emission field with LO field.[39−46] These heterodyne detection schemes often utilize sophisticated setup where the LO pulse is generated separately and then combined with the emission pulse in an interferometer, which requires stringent mechanical stability and optical alignment.[40,41] To eliminate phase drift, we designed a compact geometry which colinearly generates a LO pulse from the same probe pulse and copropagate in the exact same optical path.[44−46] Finally, the spatial resolution of TEFISH is significantly higher than typical free-space infrared spectroscopy by converting the materials' response from the long-wavelength THz pump pulses to short-wavelength TEFISH signal pulses centered around 400 nm.[47−49]

Our experimental setup is illustrated in Figure 1a. The NIR pulses are generated in dual OPAs pumped by 40 fs pulses centered at 800 nm from a mode-locked Ti:sapphire laser at a 5 kHz repetition rate. The center frequencies of the two NIR pulses ω_1 and ω_2 are independently tunable to simultaneously meet the desirable THz frequency $\omega_d = \omega_1 - \omega_2$ and the phase-matching condition.[50] The two NIR pulses with a bandwidth-limited duration of about 60 fs are stretched by high-efficiency transmission grating pairs with a matching chirp easily tuned from 0 to -10^6 fs^2. For generating THz pulses with a center frequency at 11 THz, we chose NIR pulses with wavelengths of 1392 and 1466 nm and stretched pulse duration of about 500 fs. The NIR pulses are attenuated by a neutral density filter to ensure the incident fluence is below the damage threshold of DAST of about 3 mJ/cm^2, and then loosely focused onto a DAST crystal. A small portion of the generated THz pulse is split and characterized in parallel by electro-optic (EO) sampling in a 100-μm thick GaSe using spectrally broadened and recompressed pulses centered at 800 nm.[51] The duration (defined as the full width at half-maximum of the intensity profile) of the resulting THz pulse is about 350 fs, yielding a nearly transform-limited bandwidth of about 1 THz (Figure 1b). The bandwidth of the THz pulse is tunable by changing the chirp introduced in the two NIR pulses. Broadband pulse allows us to perform broadband spectroscopy while narrowband pulse is beneficial for resonance imaging due to high spectral intensity. A large tuning range between 4 and 18 THz can be achieved by optimizing the center wavelengths of each NIR pulse (Figure 1c). Dips at certain frequencies in the spectral intensity occur due to water vapor absorption and phonon absorption in DAST, which lead to echoes in the time domain.[38,52] Purging the setup with dry nitrogen reduces the effect of water vapor absorption,[53,54] and replacing different organic crystals can remove certain phonon bands.[37] The carrier-envelope phase of the generated THz pulse is passively stabilized because the two OPAs-producing NIR pulses are seeded by the same white light continuum.[55] The phase drift is about 1 rad/h due to thermal and mechanical instabilities of the setup but can be corrected by simultaneously monitoring the EO signal of the THz pulse. We identified the optimal pumping conditions and crystal thickness to maximize the efficiency of the multilevel down-conversion by rigorously simulating the nonlinear process up to the fourth order using the optical constant of DAST (Supporting Information Section 1).[56−58] The optimal thickness of DAST for this frequency is found to be 280 μm, which is a trade-off between high-order down-conversion and THz loss, agreeing with the empirical value. We discovered that the conversion efficiency can be significantly higher in thinner crystals with moderate improvement in damage threshold, possibly achieved by cooling the crystal in an inert environment.

To enable microscopy with higher field strength at the sample position, the THz pulses are first cleaned by an 18-THz low-pass filter and then collimated, expanded, and focused to a spot size of about 200 μm, which is directly measured by a sensor array. The total power at the sample location calibrated by a THz thermopile sensor is up to 1 mW. Thus, the peak field strength focused on the sample can reach up to 1 MV/cm using NIR pump beams at DAST with a diameter of 1 mm and should linearly scale with the beam size while keeping the same fluence. Strong THz field is beneficial for fast imaging in all our samples, which are insulators or semiconductors, although it is possible that for semimetals or metals, such a field is already in the nonperturbative regime. Part of the broadband 800 nm pulse is also directed and focused onto the sample inside the THz spot for TEFISH measurement, with a spot size of 30 μm in diameter and a total power of 2 mW. To enable phase-sensitive heterodyne TEFISH measurement in centrosymmetric materials without intrinsic LO field, a 10-μm-thick beta barium borate crystal is inserted to generate copropagating pulses centered at 400 nm, with a tunable power between 0.1 nW and 1 μW under different phase matching conditions. The group velocity delay between the probe and LO pulses is compensated by a calcite crystal for heterodyne detection. To control the polarization of the 800-nm probe and the 400-nm LO field independent from the THz field without affecting the intensity and interference path, a broadband half-wave plate is placed after the calcite crystal to simultaneously rotate the polarization of both probe and LO. The TEFISH emission interferes with the LO pulse on the sample, whose temporal overlap and relative phase can be controlled with a precision of 0.1 fs and 0.5 rad, respectively, by rotating the calcite crystal with a precision of 20 arcsecond. The superposed signal is collected by an objective with long working distance (NA = 0.28). A tunable aperture is placed at the intermediate imaging plane with 50× magnification to select light emission from the desired sample area, achieving confocal microscopy. Ultimately, the signal goes through a series of band-pass filters and is collected by a photomultiplier tube. The cumulative quantum efficiency of the detection path is calibrated to be 4%.

Quantitative Phase-Sensitive TEFISH. To quantitatively obtain the TEFISH field and calculate $\chi^{(3)}$, we measure both the total homodyne TEFISH emission without interference, which yields the amplitude of $\chi^{(3)}$, and the heterodyne TEFISH signal, which provides the spectral profile of $\chi^{(3)}$. First, the homodyne TEFISH is calculated from the theoretical formalism of Powers et al.[59] Under the slowly varying envelope approximation and undepleted pump approximation, the coupled-amplitude equation for the TEFISH field in the frequency domain is

$$\frac{\mathrm{d}A_{2\omega}}{\mathrm{d}z} = \frac{3i\omega}{4cn_{2\omega}}\chi^{(3)}(\omega, \omega, \Omega)A_{\omega}^{2}A_{\mathrm{THz}}\mathrm{e}^{i\Delta \mathrm{k}z} \tag{1}$$

where A_i ($i = \omega$, 2ω, THz) is the amplitude of electric field $E_i = \frac{1}{2}A_i\mathrm{e}^{i(k_iz-\omega_it)}$ for the probe pulse, SHG, and the THz pump pulse, respectively. $\Delta k = 2k_\omega + k_{\mathrm{THz}} - k_{2\omega}$ is the wavevector mismatch. The amplitude of the TEFISH field at the exit plane is obtained by integrating eq 1 from $z = 0$ to $z = L$ (L is the thickness of the sample), yielding the intensity of the TEFISH emission:

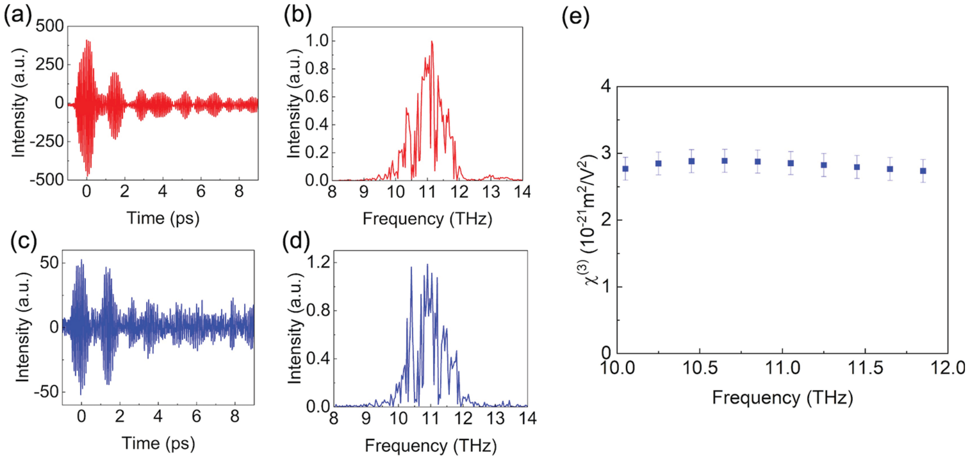

Figure 2. Spectrally resolved $\chi^{(3)}$ of the SU-8 thin film obtained from heterodyne TEFISH measurement. The time-domain (a) and frequency-domain (b) profiles of the THz pump pulse measured by electro-optic sampling in GaSe are largely replicated by those of the TEFISH signal (c,d) from the SU-8 thin film, mainly originating from the nonresonant electronic polarization. The amplitude and phase information on TEFISH are obtained by interfering with the external local oscillator field. (e) Spectrally resolved $\chi^{(3)}$ of SU-8 is nearly flat in this frequency range.

$$\begin{aligned} I_{2\omega}^{\mathrm{TEFISH}} &= \frac{1}{2}\epsilon_0 ncA_{2\omega}(\mathrm{L})^2 \\ &= \frac{9\omega^2 |\chi^{(3)}(\omega, \omega, \Omega)|^2}{4\epsilon_0^2 c^4 n_{2\omega} n_\omega^2 n_{\mathrm{THz}}} I_\omega^2 I_{\mathrm{THz}} L^2 \sin c^2(\frac{\Delta kL}{2}) \end{aligned} \tag{2}$$

However, TEFISH is usually performed in the time domain, so that the emission represents the instantaneous nonlinear polarization of the samples. The probe pulses are shorter (~30 fs in our case) than the half cycle of the THz pulses and the bandwidth of the probe pulse $\Delta\omega$ is not negligible compared with Ω. The general time-domain equation is more difficult to solve, but often the samples are much thinner than the phasing matching condition of the nonlinear mixing process, which is usually a few micrometers, so we can neglect phase mismatch and pulse walk-off. Furthermore, we can assume that the $\chi^{(3)}$ is instantaneous in the optical frequencies, i.e., the material has small dispersion within $\Delta\omega$. In this case, the instantaneous TEFISH polarization at time t is a convolution among $\chi^{(3)}$, the THz field, and the probe field as a function of the delay τ between the THz pump and the optical probe:

$$\begin{aligned} &\frac{\mathrm{d}E_{2\omega}^{\mathrm{TEFISH}}(t;\, \tau)}{\mathrm{d}z} \\ &= \frac{3i\omega}{cn_{2\omega}} \int_{-\infty}^{+\infty} \chi^{(3)}(\omega, \omega, t') \\ &\quad E_{\mathrm{THz}}(t - t' + \tau)E_\omega^2(t)\mathrm{d}t' \end{aligned} \tag{3}$$

To transform the time-domain TEFISH intensity to the frequency-domain $\chi^{(3)}$ spectrum, we can expand $\chi^{(3)}$ and E_{THz} in frequency bases and integrate out t and τ, assuming that E_{THz} is a slowly varying function in the integration range of t:

$$\begin{aligned} &\int_{-\infty}^{+\infty} I_{2\omega}^{\mathrm{TEFISH}}(\tau)\mathrm{d}\tau \\ &= \frac{9\omega^2 I_\omega^2 L^2}{4\epsilon_0^2 c^4 n_{2\omega} n_\omega^2 n_{\mathrm{THz}}} \int_{-\infty}^{+\infty} |\chi^{(3)}(\Omega)|^2 I_{\mathrm{THz}}(\Omega)\mathrm{d}\Omega \end{aligned} \tag{4}$$

Here, $I_{\mathrm{THz}}(\Omega)$ is the spectral intensity of the THz pump pulse measured by EO sampling, corrected by the response function of GaSe (Supporting Information Section 2).

Second, the heterodyne TEFISH signal interfering with an LO field $E_{2\omega}^{\mathrm{LO}}(t) \propto E_\omega^2(t) \propto I_\omega$ is obtained after deducting the LO intensity and the homodyne TEFISH intensity from the total second harmonic signal:

$$\begin{aligned} \Delta I_{2\omega}^{\mathrm{TEFISH}}(\tau) &\propto \int_{-\infty}^{+\infty} [|E_{2\omega}^{\mathrm{TEFISH}}(t;\, \tau) + E_{2\omega}^{\mathrm{LO}}(t)|^2 \\ &\quad - |E_{2\omega}^{\mathrm{LO}}(t)|^2 - |E_{2\omega}^{\mathrm{TEFISH}}(t;\, \tau)|^2]\mathrm{d}t \\ &\propto I_\omega \int \chi^{(3)}(\omega, \omega, t')E_{\mathrm{THz}}(t - t' + \tau)\mathrm{d}t' \end{aligned} \tag{5}$$

It is possible that the THz pump modulates the sample's transmission to the LO and introduces a false signal. For all our samples, we also measured transient transmission by filtering out the 800-nm probe pulse from the LO and found the signal is negligible compared with TEFISH. Although the heterodyne TEFISH signal is not quantitative in amplitude due to its sensitivity to the spatial−temporal overlap of the TEFISH and LO pulses, we can still obtain the spectral profile of $\chi^{(3)}$ by Fourier transforming eq 5:

$$\chi^{(3)}(\Omega) \propto \frac{\mathcal{F}[\Delta I_{2\omega}^{\mathrm{TEFISH}}(\tau)]}{I_{\mathrm{THz}}(\Omega)} \tag{6}$$

In many cases, we only need to measure $I_{2\omega}^{\mathrm{TEFISH}}(\tau)$ and can separate the Fourier spectrum into 0, Ω, and 2Ω frequency components as long as the THz pump is narrowband. The Ω-frequency component yields $\Delta I_{2\omega}^{\mathrm{TEFISH}}(\tau)$ and $\chi^{(3)}(\Omega)$ in arbitrary units, and then the 0-frequency component allows us to normalize the amplitude of $\chi^{(3)}(\Omega)$. But for weakly nonlinear samples, the homodyne TEFISH is measured separately without LO. The signal-to-noise ratio (SNR) of this measurement is independent of LO field because both the signal and the shot noise are proportional to the LO field. Rather, SNR is proportional to the materials' $\chi^{(3)}$, the sample volume, and the strength of the pump THz field. Hence, our heterodyne TEFISH microscopy with a larger THz field strength offers a lower detection limit for microscopic samples.

Probing Vibrational Resonance in Thin Films. As a proof of concept, we first measured the $\chi^{(3)}$ spectrum of the polymer thin film SU-8. SU-8 is a widely used photoresist for micromachining and microelectronic fabrication. It has relatively low loss and no prominent vibrational resonances

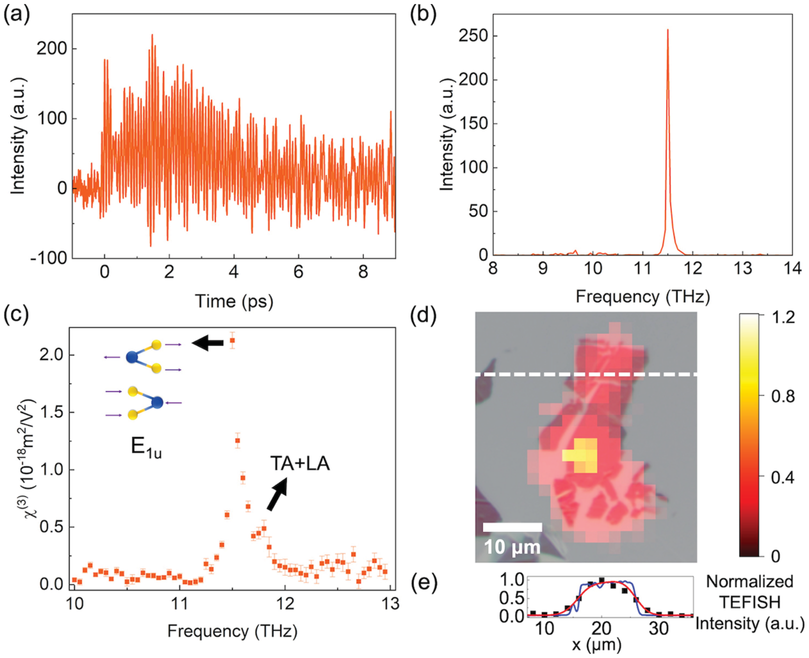

Figure 3. Coherent phonon displacement in 2H-MoS_2 ultrathin film revealed by heterodyne TEFISH in (a) time domain (b) frequency domain. (c) The spectrally resolved $\chi^{(3)}$ exhibits a major peak at 11.5 THz and a minor feature at 11.8 THz, corresponding to the resonantly excited, infrared-active phonon mode E_{1u} and a two-phonon process, respectively. (d) The TEFISH map overlaid with the optical microscope image of the MoS_2 shows good agreement and verifies a subwavelength spatial resolution about 7 μm with respect to the infrared wavelength of 26 μm. (e) The TEFISH signal (black dots) and the Gaussian convolution (red curve) of the optical image (blue curve) at the location indicated by the white dashed line cut in (d).

in the frequency range of 10−12 THz, compared with other common epoxy-based photo- and electron-beam resists, and thus is useful for THz photonics. The 1.8-μm-thick SU-8 was spin-coated onto a fused silica substrate, which has been verified to give negligible TEFISH signal under our experimental conditions. The main reasons for weak TEFISH in silica are the large electronic band gap compared with SU-8, the lack of well-defined phonon resonances at this frequency range, and poor phase-matching conditions. By contrast, bulk sapphire gives a gigantic TEFISH signal owing to phase matching, and thus sapphire is not suitable as substrate material (Supporting Information Section 3). We first measured the THz field in time and frequency domains through EO sampling in GaSe (Figure 2a,b). The beat, compared with the trace measured in a dry nitrogen environment (Figure 1b), originates from water absorption lines as seen from the Fourier spectrum. These lines do not affect our measurements of $\chi^{(3)}$ spectra, which are normalized by the THz spectra in the present study as long as the spectral intensity is finite. The robustness of our method against absorbing medium makes it more versatile to study solutions or biological specimens, although a vacuum chamber may be implemented to improve SNR for solid materials in the future. We then measured the time-resolved TEFISH of the SU-8 film as a function of probe delay with respect to the THz excitation (Figure 2c). Since the LO field is much stronger than TEFISH, the symmetric interference term dominates the signal. It is evident that the TEFISH spectrum of the SU-8 thin film (Figure 2d) follows that of the THz pump pulse, which suggests no resonance exists in this frequency range. Using optical parameters determined by previous studies on SU-8,[60,61] we calculated the spectrally resolved $\chi^{(3)}$ (Figure 2e). The $\chi^{(3)}$ shows a slow-varying trend with no apparent vibrational resonance, as expected, and mainly comes from nonresonant electronic contributions in this frequency range. The averaged value of $\chi^{(3)}$ is determined to be 2.8×10^{-21} m^2 V^{-2}, which matches with previously reported value in the visible frequencies.[62]

We further demonstrated the ability to quantify phonon-resonance-induced $\chi^{(3)}$ with an ultrathin flake of 2H-MoS_2. 2H-MoS_2 containing an even number of layers is centrosymmetric and has an infrared-active phonon mode E_{1u} centered at around 11.5 THz, which is Raman-inactive and cannot be measured by conventional Raman spectroscopy. The MoS_2 flake was exfoliated on polydimethylsiloxane and transferred to a fused silica substrate. Its thickness of 12 nm (20 layers) was determined by absorption spectroscopy and further confirmed by the weakness of SHG. Through TEFISH, we clearly observed the oscillatory time-domain signal (Figure 3a), which directly represents the coherent atomic displacement that causes inversion symmetry breaking. The asymmetric waveform arises from the non-negligible quadratic term of the TEFISH emission but does not affect the spectral analysis. The spectral domain signal is dominated by a sharp phonon resonance above the small baseline from the nonresonant electronic contributions (Figure 3b). We calculated the maximum $\chi^{(3)}$ to be 2.1×10^{-18} m^2/V^2, 3 orders of magnitude larger than that of SU-8 due to the double resonance from the phonons and the excitons. The nonresonant baseline of $\chi^{(3)}$ is on the order of 10^{-19} m^2/V^2, which agrees with the value of nonresonant optical $\chi^{(3)}$ reported previously.[63] Note that the feature at around 11.8 THz can be attributed to two-phonon processes according to previous IR absorption measurement and spectral analysis.[64,65] The observation shows coherent atomic displacement arising from two correlated modes excited by one photon, as opposed to nonlinear phononics, where one

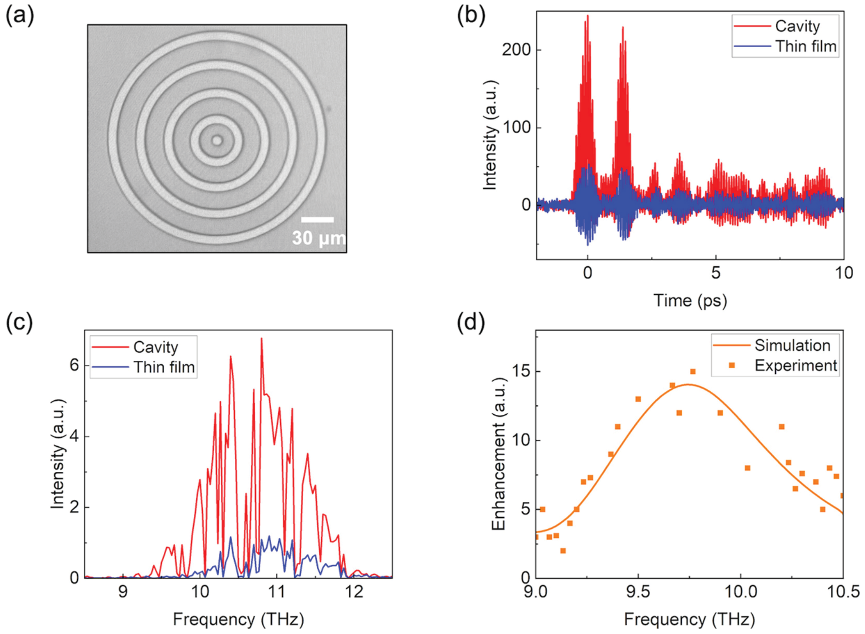

Figure 4. Subdiffraction spectroscopy demonstrated by measuring the THz electric field in a subwavelength resonator. (a) The optical image of SU-8 disk (3-μm-thick and 9 μm in diameter) resonator on CaF_2 substrate at the center of the phonon−polariton grating coupler. Comparing the temporal (b) and spectral (c) response of the TEFISH signal from the resonator and the SU-8 thin film. The signal from the resonator is enhanced in amplitude and shifted in frequency. (d) The normalized TEFISH spectrum (dot) matches the simulated field enhancement factor averaged over the central disk resonator (line), showing that the spectrum is taken with a high spatial resolution commensurate with the dimension of the disk resonator.

phonon mode is excited by two photons. The sample has a total volume of 10 μm^3 and yields a SNR of 200 in the $\chi^{(3)}$ spectrum, meaning that the current operation condition can probe time-domain atomic motion in samples with a volume as small as 0.05 μm^3 (1.5×10^{-15} mol bonds). Note that for such small samples, we can no longer quantify the magnitude of $\chi^{(3)}$ because the TEFISH emission without interference would be too weak, but the $\chi^{(3)}$ spectrum is still measurable by the interference signal. Compared to homodyne CARS which is quadratic to the sample's volume and often runs at the risk of sample damage, the THz excitation to generate TEFISH is still quite moderate (average power of 1 W/cm^2) and has much room to increase. Such sensitivity far exceeds that of conventional far-field, table-top FTIR microscopy, which is typically on the order of 10^{-12} mol. Although it does not reach the sensitivity of near-field, synchrotron-based infrared nanospectroscopy (10^{-19} mol)[66] or picocavity-enhanced Raman spectroscopy (10^{-23} mol),[67] TEFISH has the benefit of directly visualizing the structure-induced hyperpolarizability, as well as revealing coherence and nonlinear selection rules. Therefore, TEFISH could be potentially useful for characterizing the ultrafast dynamics of ultrathin molecular layers, dilute solutions, and low-density defects.

To illustrate the spatial resolution of the confocal microscope setup, we performed 2D TEFISH mapping of an ultrathin MoS_2 flake. The sample has a lateral size about 10 μm, which is too small for commercial FTIR microscopy, and its phonon resonance frequency of 11.5 THz is also below the range of common FTIR. The selection aperture was reduced to about 150 μm, so only the signal from a spot with a diameter of 3 μm on the sample could be collected. By scanning the sample, we obtained the TEFISH image of the MoS_2 flake overlaid on its optical image, and the two agree well (Figure 3d). The shape of the flake is well-defined, and the nonuniformity at the center of the sample is distinguished, although the cracks of up to 2 μm in width cannot be resolved. We applied Gaussian blur to the optical image to simulate the TEFISH image and estimate that the resolution is around 7 μm (Supporting Information Section 4). The diffraction limited resolution is $R_{\text{Abbe}} = \frac{1.22\,\lambda_{2\omega}}{\text{NA}} = 1.7\ \mu\text{m}$ in theory, yet there is a trade-off between imaging speed and resolution in the current setup.

Probing Photonic Resonance in Subwavelength Microstructures. To further demonstrate the spatial resolution of heterodyne TEFISH microscopy for probing subwavelength infrared photonics, we compared the $\chi^{(3)}$ of a THz phonon−polariton resonator made from SU-8 grating on CaF_2 and the $\chi^{(3)}$ of a flat SU-8 thin film. When the materials' $\chi^{(3)}$ is known, the TEFISH signal can tell the strength of the enhanced local THz field, or alternatively, a larger "effective" $\chi^{(3)}$ in the resonator if we assume the free-space THz field strength to calculate the TEFISH signal. We chose the bull's eye resonator geometry, first introduced in the context of surface plasmon polaritons, and applied the same principle to SPhP.[68,69] We implemented the methodology of numerical optimization and fabrication previously reported for $SrTiO_3$ SPhP resonators with another ionic crystal CaF_2, whose dielectric function is negative between 8 and 13 THz and can support SPhP in this frequency range.[69] Briefly, we simulated the electric field response of the resonator with a finite-difference time-domain method (Lumerical). The field enhancement with respect to the incoming THz pulses with a Gaussian beam profile is optimized by three geometrical parameters: the periodicity of the concentric ring grating, the diameter of the central disk, and the thickness of the SU-8 layer. The gratings with a periodicity of 25 μm couple the incident THz field into propagating SPhPs, which then focuses on a subwavelength central disk with a diameter of 9 μm

https://doi.org/10.1021/acsphotonics.3c00787
ACS Photonics 2024, 11, 33−41

(Figure 4a). The resonance frequency of the structure was found to be 9.7 THz (Supporting Information, Section 5). The optical dielectric functions of SU-8 and CaF_2 used in the simulation were taken from previous literature.[70,71] The THz spectral intensity can be measured by TEFISH and is expected to be enhanced by up to 13 times on average inside the SU-8 disk.

In the experiment, we collected all signals coming from the central disk area and indeed observed significant enhancement of the TEFISH signal (Figure 4b) with marked frequency shift from the incident THz excitation (Figure 4c). We also verified that a bare crystalline CaF_2 substrate has a negligible signal, so the spectral change is solely attributed to the SU-8 part of the resonator. The time-domain signal is asymmetric, again because the quadratic term is no longer negligible when the TEFISH signal is greatly enhanced, adding a positive envelope to the signal. By normalizing the TEFISH spectrum of the resonator with that of the SU-8 thin film on a fused silica substrate, we can obtain the spectrally resolved field enhancement $E^2(\omega)/E_0^2(\omega)$ averaged over the central SU-8 disk, which agrees very well with the numerical simulation (Figure 4d). Therefore, we can conclude that the disk resonator is well-resolved because, if otherwise, there would be no $\chi^{(3)}$ from SU-8 in the trench surrounding the resonator, and the average signal would greatly reduce. Higher resolution is in principle achievable with larger NA, but currently limited by the geometry of the setup, where samples are mounted in cryostat that supports low-temperature infrared imaging.

CONCLUSIONS

To summarize, we present coherent heterodyne TEFISH microscopy that quantitatively probes third-order optical nonlinearity of materials with better spatial resolution for the first time, to the best of our knowledge. Intense and frequency-tunable THz source with field strength on the order of MV/cm is produced by chirped-pulse DFG in DAST guided by a model of high-order nonlinear frequency mixing. Heterodyne measurement with a collinear LO provides both the amplitude and phase information on time-domain TEFISH that yield $\chi^{(3)}$ spectra in centrosymmetric materials. Moreover, the signal scales linearly with $\chi^{(3)}$ and the sample volume, leading to better sensitivity for small samples. Using the heterodyne TEFISH protocol, we experimentally quantify the $\chi^{(3)}$ of SU-8 thin film in 10−12 THz. We further show the spectral sensitivity and spatial resolution is sufficient to reveal vibrational or photonic resonances in subwavelength samples such as ultrathin semiconductors and surface phonon−polariton resonators. Thus, TEFISH spectroscopic microscopy provides an exciting tool for label-free nonlinear imaging of atomic displacement in materials, which may have broad applications in investigating far-infrared photonics, solid-state quantum materials, and chemical reaction dynamics.

ASSOCIATED CONTENT

Supporting Information

The Supporting Information is available free of charge at https://pubs.acs.org/doi/10.1021/acsphotonics.3c00787.

Additional experimental details on terahertz generation and characterization, optical imaging, materials properties, and device simulations (PDF)

AUTHOR INFORMATION

Corresponding Author

Hanyu Zhu − *Department of Materials Science and NanoEngineering, Rice University, Houston, Texas 77005, United States;* orcid.org/0000-0003-3376-5352; Email: hanyu.zhu@rice.edu

Authors

Tong Lin − *Department of Materials Science and NanoEngineering, Rice University, Houston, Texas 77005, United States*
Rui Xu − *Department of Materials Science and NanoEngineering, Rice University, Houston, Texas 77005, United States*
Xiaotong Chen − *Department of Materials Science and NanoEngineering, Rice University, Houston, Texas 77005, United States*
Yuxuan Guan − *Department of Materials Science and NanoEngineering, Rice University, Houston, Texas 77005, United States*
Mingxing Yao − *Department of Materials Science and NanoEngineering, Rice University, Houston, Texas 77005, United States*
Junhao Zhang − *Department of Materials Science and NanoEngineering, Rice University, Houston, Texas 77005, United States*
Xinwei Li − *Department of Electrical and Computer Engineering, Rice University, Houston, Texas 77005, United States*

Complete contact information is available at: https://pubs.acs.org/10.1021/acsphotonics.3c00787

Funding

This work is supported by the U.S. National Science Foundation (DMR-2240106) and Robert A. Welch Foundation (C-2128).

Notes

The authors declare no competing financial interest.

ACKNOWLEDGMENTS

We thank Swiss Terahertz GmbH for providing organic crystals with various composition and thicknesses to optimize THz generation.

REFERENCES

(1) Tipping, W. J.; Lee, M.; Serrels, A.; Brunton, V. G.; Hulme, A. N. Stimulated Raman Scattering Microscopy: An Emerging Tool for Drug Discovery. *Chem. Soc. Rev.* **2016**, *45* (8), 2075−2089.

(2) Hu, F.; Shi, L.; Min, W. Biological Imaging of Chemical Bonds by Stimulated Raman Scattering Microscopy. *Nat. Methods* **2019**, *16* (9), 830−842.

(3) Casacio, C. A.; Madsen, L. S.; Terrasson, A.; Waleed, M.; Barnscheidt, K.; Hage, B.; Taylor, M. A.; Bowen, W. P. Quantum-Enhanced Nonlinear Microscopy. *Nature* **2021**, *594* (7862), 201−206.

(4) Ziegler, L. D. Hyper-Raman Spectroscopy. *J. Raman Spectrosc.* **1990**, *21* (12), 769−779.

(5) Sheik-Bahae, M.; Said, A. A.; Wei, T.-H.; Hagan, D. J.; Van Stryland, E. W. Sensitive Measurement of Optical Nonlinearities Using a Single Beam. *IEEE J. Quantum Electron.* **1990**, *26* (4), 760−769.

(6) Nahata, A.; Heinz, T. F. Detection of Freely Propagating Terahertz Radiation by Use of Optical Second-Harmonic Generation. *Opt. Lett.* **1998**, *23* (1), 67.

(7) Dai, J.; Xie, X.; Zhang, X.-C. Detection of Broadband Terahertz Waves with a Laser-Induced Plasma in Gases. *Phys. Rev. Lett.* **2006**, *97* (10), No. 103903.

(8) Chen, J.; Han, P.; Zhang, X.-C. Terahertz-Field-Induced Second-Harmonic Generation in a Beta Barium Borate Crystal and Its Application in Terahertz Detection. *Appl. Phys. Lett.* **2009**, *95* (1), No. 011118.

(9) Cheng, L. T.; Tam, W.; Stevenson, S. H.; Meredith, G. R.; Rikken, G.; Marder, S. R. Experimental Investigations of Organic Molecular Nonlinear Optical Polarizabilities. 1. Methods and Results on Benzene and Stilbene Derivatives. *J. Phys. Chem.* **1991**, *95* (26), 10631−10643.

(10) Clays, K.; Persoons, A. Hyper-Rayleigh Scattering in Solution. *Phys. Rev. Lett.* **1991**, *66* (23), 2980−2983.

(11) Dhillon, S. S.; Vitiello, M. S.; Linfield, E. H.; Davies, A. G.; Hoffmann, M. C.; Booske, J.; Paoloni, C.; Gensch, M.; Weightman, P.; Williams, G. P.; Castro-Camus, E.; Cumming, D. R. S.; Simoens, F.; Escorcia-Carranza, I.; Grant, J.; Lucyszyn, S.; Kuwata-Gonokami, M.; Konishi, K.; Koch, M.; Schmuttenmaer, C. A.; et al. The 2017 Terahertz Science and Technology Roadmap. *J. Phys. D: Appl. Phys.* **2017**, *50* (4), No. 043001.

(12) Leitenstorfer, A.; Moskalenko, A. S.; Kampfrath, T.; Kono, J.; Castro-Camus, E.; Peng, K.; Qureshi, N.; Turchinovich, D.; Tanaka, K.; Markelz, A.; Havenith, M.; Hough, C.; Joyce, H. J.; Padilla, W.; Zhou, B.; Kim, K.-Y.; Zhang, X.-C.; Jepsen, P. U.; Dhillon, S.; Vitiello, M. S.; et al. The 2023 Terahertz Science and Technology Roadmap. *J. Phys. D: Appl. Phys.* **2023**, *56*, 223001.

(13) Först, M.; Manzoni, C.; Kaiser, S.; Tomioka, Y.; Tokura, Y.; Merlin, R.; Cavalleri, A. Nonlinear Phononics as an Ultrafast Route to Lattice Control. *Nat. Phys.* **2011**, *7* (11), 854−856.

(14) Kozina, M.; Fechner, M.; Marsik, P.; van Driel, T.; Glownia, J. M.; Bernhard, C.; Radovic, M.; Zhu, D.; Bonetti, S.; Staub, U.; Hoffmann, M. C. Terahertz-Driven Phonon Upconversion in $SrTiO_3$. *Nat. Phys.* **2019**, *15* (4), 387−392.

(15) Disa, A. S.; Fechner, M.; Nova, T. F.; Liu, B.; Först, M.; Prabhakaran, D.; Radaelli, P. G.; Cavalleri, A. Polarizing an Antiferromagnet by Optical Engineering of the Crystal Field. *Nat. Phys.* **2020**, *16* (9), 937−941.

(16) Stupakiewicz, A.; Davies, C. S.; Szerenos, K.; Afanasiev, D.; Rabinovich, K. S.; Boris, A. V.; Caviglia, A.; Kimel, A. V.; Kirilyuk, A. Ultrafast Phononic Switching of Magnetization. *Nat. Phys.* **2021**, *17* (4), 489−492.

(17) Luo, J.; Lin, T.; Zhang, J.; Chen, X.; Blackert, E. R.; Xu, R.; Yakobson, B. I.; Zhu, H. Large Effective Magnetic Fields from Chiral Phonons in Rare-Earth Halides. *Science* 2023, *382*(6671), 698-702 DOI: 10.1126/science.adi9601.

(18) Liu, B.; Först, M.; Fechner, M.; Nicoletti, D.; Porras, J.; Loew, T.; Keimer, B.; Cavalleri, A. Pump Frequency Resonances for Light-Induced Incipient Superconductivity in $YBa_2Cu_3O_{6.5}$. *Phys. Rev. X* **2020**, *10* (1), No. 011053.

(19) Budden, M.; Gebert, T.; Buzzi, M.; Jotzu, G.; Wang, E.; Matsuyama, T.; Meier, G.; Laplace, Y.; Pontiroli, D.; Riccò, M.; Schlawin, F.; Jaksch, D.; Cavalleri, A. Evidence for Metastable Photo-Induced Superconductivity in K_3C_{60}. *Nat. Phys.* **2021**, *17* (5), 611−618.

(20) Von Hoegen, A.; Fechner, M.; Först, M.; Taherian, N.; Rowe, E.; Ribak, A.; Porras, J.; Keimer, B.; Michael, M.; Demler, E.; Cavalleri, A. Amplification of Superconducting Fluctuations in Driven $YBa_2Cu_3O_{6+x}$. *Phys. Rev. X* **2022**, *12* (3), No. 031008.

(21) Kaindl, R. A.; Wurm, M.; Reimann, K.; Hamm, P.; Weiner, A. M.; Woerner, M. Generation, Shaping, and Characterization of Intense Femtosecond Pulses Tunable from 3 to 20 μm. *J. Opt. Soc. Am. B* **2000**, *17* (12), 2086.

(22) Danielson, J. R.; Jameson, A. D.; Tomaino, J. L.; Hui, H.; Wetzel, J. D.; Lee, Y.-S.; Vodopyanov, K. L. Intense Narrow Band Terahertz Generation via Type-II Difference-Frequency Generation in ZnTe Using Chirped Optical Pulses. *J. Appl. Phys.* **2008**, *104* (3), No. 033111.

(23) Knorr, M.; Raab, J.; Tauer, M.; Merkl, P.; Peller, D.; Wittmann, E.; Riedle, E.; Lange, C.; Huber, R. Phase-Locked Multi-Terahertz Electric Fields Exceeding 13 MV/cm at a 190 kHz Repetition Rate. *Opt. Lett.* **2017**, *42* (21), 4367.

(24) Cartella, A.; Nova, T. F.; Oriana, A.; Cerullo, G.; Först, M.; Manzoni, C.; Cavalleri, A. Narrowband Carrier-Envelope Phase Stable Mid-Infrared Pulses at Wavelengths beyond 10 μm by Chirped-Pulse Difference Frequency Generation. *Opt. Lett.* **2017**, *42* (4), 663.

(25) Liu, B.; Bromberger, H.; Cartella, A.; Gebert, T.; Först, M.; Cavalleri, A. Generation of Narrowband, High-Intensity, Carrier-Envelope Phase-Stable Pulses Tunable between 4 and 18 THz. *Opt. Lett.* **2017**, *42* (1), 129.

(26) He, Y.; Wang, Y.; Xu, D.; Nie, M.; Yan, C.; Tang, L.; Shi, J.; Feng, J.; Yan, D.; Liu, H.; Teng, B.; Feng, H.; Yao, J. High-Energy and Ultra-Wideband Tunable Terahertz Source with DAST Crystal via Difference Frequency Generation. *Appl. Phys. B: Lasers Opt.* **2018**, *124* (1), 16.

(27) Vicario, C.; Trisorio, A.; Allenspach, S.; Rüegg, C.; Giorgianni, F. Narrow-Band and Tunable Intense Terahertz Pulses for Mode-Selective Coherent Phonon Excitation. *Appl. Phys. Lett.* **2020**, *117* (10), 101101.

(28) Ovchinnikov, A. V.; Chefonov, O. V.; Agranat, M. B.; Fortov, V. E.; Jazbinsek, M.; Hauri, C. P. Generation of Strong-Field Spectrally Tunable Terahertz Pulses. *Opt. Express* **2020**, *28* (23), 33921.

(29) Seo, M.; Mun, J.-H.; Heo, J.; Kim, D. E. High-Efficiency near-Infrared Optical Parametric Amplifier for Intense, Narrowband THz Pulses Tunable in the 4 to 19 THz Region. *Sci. Rep.* **2022**, *12* (1), 16273.

(30) Cook, D. J.; Chen, J. X.; Morlino, E. A.; Hochstrasser, R. M. Terahertz-Field-Induced Second-Harmonic Generation Measurements of Liquid Dynamics. *Chem. Phys. Lett.* **1999**, *309* (3−4), 221−228.

(31) Tokman, M.; Bodrov, S. B.; Sergeev, Y. A.; Korytin, A. I.; Oladyshkin, I.; Wang, Y.; Belyanin, A.; Stepanov, A. N. Second Harmonic Generation in Graphene Dressed by a Strong Terahertz Field. *Phys. Rev. B* **2019**, *99* (15), No. 155411.

(32) Grishunin, K. A.; Ilyin, N. A.; Sherstyuk, N. E.; Mishina, E. D.; Kimel, A.; Mukhortov, V. M.; Ovchinnikov, A. V.; Chefonov, O. V.; Agranat, M. B. THz Electric Field-Induced Second Harmonic Generation in Inorganic Ferroelectric. *Sci. Rep.* **2017**, *7* (1), 687.

(33) Li, X.; Qiu, T.; Zhang, J.; Baldini, E.; Lu, J.; Rappe, A. M.; Nelson, K. A. Terahertz Field−Induced Ferroelectricity in Quantum Paraelectric $SrTiO_3$. *Science* **2019**, *364* (6445), 1079−1082.

(34) Huang, H.; Song, L.; Tancoene-Deiean, N.; Klemke, N.; Rubio, A.; Kartner, F. X.; Miicke, O. D. Ultrafast Control of Even-Order Harmonic Generation from Solids by an Intense Terahertz Field. In *2018 43rd International Conference on Infrared, Millimeter, and Terahertz Waves (IRMMW-THz)*; Nagoya: IEEE, 2018; pp 1−2, DOI: 10.1109/IRMMW-THz.2018.8510220.

(35) von Hoegen, A.; Mankowsky, R.; Fechner, M.; Först, M.; Cavalleri, A. Probing the Interatomic Potential of Solids with Strong-Field Nonlinear Phononics. *Nature* **2018**, *555* (7694), 79−82.

(36) Okorogu, A. O.; Mirov, S. B.; Lee, W.; Crouthamel, D. I.; Jenkins, N.; Dergachev, A. Y.; Vodopyanov, K. L.; Badikov, V. V. Tunable Middle Infrared Downconversion in GaSe and $AgGaS_2$. *Opt. Commun.* **1998**, *155* (4−6), 307−312.

(37) Jazbinsek, M.; Puc, U.; Abina, A.; Zidansek, A. Organic Crystals for THz Photonics. *Appl. Sci.* **2019**, *9* (5), 882.

(38) Notake, T.; Nawata, K.; Kawamata, H.; Matsukawa, T.; Qi, F.; Minamide, H. Development of an Ultra-Widely Tunable DFG-THz Source with Switching between Organic Nonlinear Crystals Pumped with a Dual-Wavelength BBO Optical Parametric Oscillator. *Opt. Express* **2012**, *20* (23), 25850.

(39) Brixner, T.; Stiopkin, I. V.; Fleming, G. R. Tunable Two-Dimensional Femtosecond Spectroscopy. *Opt. Lett.* **2004**, *29* (8), 884.

(40) Stiopkin, I. V.; Jayathilake, H. D.; Bordenyuk, A. N.; Benderskii, A. V. Heterodyne-Detected Vibrational Sum Frequency Generation Spectroscopy. *J. Am. Chem. Soc.* **2008**, *130* (7), 2271−2275.

(41) Chen, X.; Hua, W.; Huang, Z.; Allen, H. C. Interfacial Water Structure Associated with Phospholipid Membranes Studied by Phase-Sensitive Vibrational Sum Frequency Generation Spectroscopy. *J. Am. Chem. Soc.* **2010**, *132* (32), 11336−11342.

(42) Shen, Y. R. Phase-Sensitive Sum-Frequency Spectroscopy. *Annu. Rev. Phys. Chem.* **2013**, *64* (1), 129−150.

(43) Han, Y.; Raghunathan, V.; Feng, R.; Maekawa, H.; Chung, C.-Y.; Feng, Y.; Potma, E. O.; Ge, N.-H. Mapping Molecular Orientation with Phase Sensitive Vibrationally Resonant Sum-Frequency Generation Microscopy. *J. Phys. Chem. B* **2013**, *117* (20), 6149−6156.

(44) Xu, B.; Wu, Y.; Sun, D.; Dai, H.-L.; Rao, Y. Stabilized Phase Detection of Heterodyne Sum Frequency Generation for Interfacial Studies. *Opt. Lett.* **2015**, *40* (19), 4472.

(45) Wang, H.; Gao, T.; Xiong, W. Self-Phase-Stabilized Heterodyne Vibrational Sum Frequency Generation Microscopy. *ACS Photonics* **2017**, *4* (7), 1839−1845.

(46) Garling, T.; Campen, R. K.; Wolf, M.; Thämer, M. A General Approach To Combine the Advantages of Collinear and Noncollinear Spectrometer Designs in Phase-Resolved Second-Order Nonlinear Spectroscopy. *J. Phys. Chem. A* **2019**, *123* (51), 11022−11030.

(47) Cheng, J.-X.; Xie, X. S. Coherent Anti-Stokes Raman Scattering Microscopy: Instrumentation, Theory, and Applications. *J. Phys. Chem. B* **2004**, *108* (3), 827−840.

(48) Chung, C.-Y.; Potma, E. O. Biomolecular Imaging with Coherent Nonlinear Vibrational Microscopy. *Annu. Rev. Phys. Chem.* **2013**, *64* (1), 77−99.

(49) Kiessling, R.; Tong, Y.; Giles, A. J.; Gewinner, S.; Schöllkopf, W.; Caldwell, J. D.; Wolf, M.; Paarmann, A. Surface Phonon Polariton Resonance Imaging Using Long-Wave Infrared-Visible Sum-Frequency Generation Microscopy. *ACS Photonics* **2019**, *6* (11), 3017−3023.

(50) Vicario, C.; Jazbinsek, M.; Ovchinnikov, A. V.; Chefonov, O. V.; Ashitkov, S. I.; Agranat, M. B.; Hauri, C. P. High Efficiency THz Generation in DSTMS, DAST and OH1 Pumped by Cr:Forsterite Laser. *Opt. Express* **2015**, *23* (4), 4573.

(51) Lu, C.-H.; Tsou, Y.-J.; Chen, H.-Y.; Chen, B.-H.; Cheng, Y.-C.; Yang, S.-D.; Chen, M.-C.; Hsu, C.-C.; Kung, A. H. Generation of Intense Supercontinuum in Condensed Media. *Optica* **2014**, *1* (6), 400.

(52) Gordon, I. E.; Rothman, L. S.; Hargreaves, R. J.; Hashemi, R.; Karlovets, E. V.; Skinner, F. M.; Conway, E. K.; Hill, C.; Kochanov, R. V.; Tan, Y.; Wcisło, P.; Finenko, A. A.; Nelson, K.; Bernath, P. F.; Birk, M.; Boudon, V.; Campargue, A.; Chance, K. V.; Coustenis, A.; Drouin, B. J.; et al. The HITRAN2020 Molecular Spectroscopic Database. *J. Quant. Spectrosc. Radiat. Transfer* **2022**, *277*, No. 107949.

(53) Grischkowsky, D.; Keiding, S.; van Exter, M.; Fattinger, Ch. Far-Infrared Time-Domain Spectroscopy with Terahertz Beams of Dielectrics and Semiconductors. *J. Opt. Soc. Am. B* **1990**, *7* (10), 2006.

(54) Lu, M.; Shen, J.; Li, N.; Zhang, Y.; Zhang, C.; Liang, L.; Xu, X. Detection and Identification of Illicit Drugs Using Terahertz Imaging. *J. Appl. Phys.* **2006**, *100* (10), 103104.

(55) Manzoni, C.; Cerullo, G.; De Silvestri, S. Ultrabroadband Self-Phase-Stabilized Pulses by Difference-Frequency Generation. *Opt. Lett.* **2004**, *29* (22), 2668.

(56) Sutherland, R. L.; McLean, D. G.; Kirkpatrick, S. *Handbook of Nonlinear Optics*, 2nd ed., rev. expanded; Optical engineering; Marcel Dekker: New York, 2003.

(57) Cunningham, P. D.; Hayden, L. M. Optical Properties of DAST in the THz Range. *Opt. Express* **2010**, *18* (23), 23620.

(58) Montemezzani, G.; Alonzo, M.; Coda, V.; Jazbinsek, M.; Günter, P. Running Electric Field Gratings for Detection of Coherent Radiation. *J. Opt. Soc. Am. B* **2015**, *32* (6), 1078.

(59) Powers, P. E.; Haus, J. W. *Fundamentals of Nonlinear Optics*, second ed.; CRC Press, Taylor & Francis Group: Boca Raton, 2017.

(60) Piruska, A.; Bhagat, A. A. S.; Zhou, K.; Peterson, E. T. K.; Papautsky, I.; Seliskar, C. J. *Characterization of SU-8 Optical Multimode Waveguides for Integrated Optics and Sensing on Microchip Devices*; Papautsky, I., Wang, W., Eds.; San Jose, CA, 2006; p 611207, DOI: 10.1117/12.655667.

(61) Ashraf, S.; Niskanen, I.; Kanyathare, B.; Vartiainen, E.; Mattsson, C.; Heikkilä, R.; Thungström, G. Determination of Complex Refractive Index of SU-8 by Kramers−Kronig Dispersion Relation Method at the Wavelength Range 2.5−22.0 Mm. *J. Quant. Spectrosc. Radiat. Transfer* **2019**, *224*, 309−311.

(62) Antropov, I. M.; Chizhov, A. S.; Abrashitova, K. A.; Bessonov, V. O.; Fedyanin, A. A. Third Harmonic Generation from Polymer Nanocomposite with Embedded CdSe Quantum Dots. *J. Phys.: Conf. Ser.* **2020**, *1461* (1), No. 012006.

(63) Woodward, R. I.; Murray, R. T.; Phelan, C. F.; de Oliveira, R. E. P.; Runcorn, T. H.; Kelleher, E. J. R.; Li, S.; de Oliveira, E. C.; Fechine, G. J. M.; Eda, G.; de Matos, C. J. S. Characterization of the Second- and Third-Order Nonlinear Optical Susceptibilities of Monolayer MoS_2 Using Multiphoton Microscopy. *2D Mater.* **2016**, *4* (1), No. 011006.

(64) Wilson, J. A.; Yoffe, A. D. The Transition Metal Dichalcogenides Discussion and Interpretation of the Observed Optical, Electrical and Structural Properties. *Adv. Phys.* **1969**, *18* (73), 193−335.

(65) Livneh, T.; Spanier, J. E. A Comprehensive Multiphonon Spectral Analysis in MoS_2. *2D Mater.* **2015**, *2* (3), No. 035003.

(66) Bechtel, H. A.; Muller, E. A.; Olmon, R. L.; Martin, M. C.; Raschke, M. B. Ultrabroadband Infrared Nanospectroscopic Imaging. *Proc. Natl. Acad. Sci. U. S. A.* **2014**, *111* (20), 7191−7196.

(67) Benz, F.; Schmidt, M. K.; Dreismann, A.; Chikkaraddy, R.; Zhang, Y.; Demetriadou, A.; Carnegie, C.; Ohadi, H.; de Nijs, B.; Esteban, R.; Aizpurua, J.; Baumberg, J. J. Single-Molecule Optomechanics in "Picocavities". *Science* **2016**, *354* (6313), 726−729.

(68) Lezec, H. J.; Degiron, A.; Devaux, E.; Linke, R. A.; Martin-Moreno, L.; Garcia-Vidal, F. J.; Ebbesen, T. W. Beaming Light from a Subwavelength Aperture. *Science* **2002**, *297* (5582), 820−822.

(69) Xu, R.; Lin, T.; Luo, J.; Chen, X.; Blackert, E. R.; Moon, A. R.; JeBailey, K. M.; Zhu, H. Phonon Polaritonics in Broad Terahertz Frequency Range with Quantum Paraelectric $SrTiO_3$. *Adv. Mater.* **2023**, *35* (32), No. 2302974.

(70) Kaiser, W.; Spitzer, W. G.; Kaiser, R. H.; Howarth, L. E. Infrared Properties of CaF_2, SrF_2, and BaF_2. *Phys. Rev.* **1962**, *127* (6), 1950−1954.

(71) Motaharifar, E.; Pierce, R. G.; Islam, R.; Henderson, R.; Hsu, J. W. P.; Lee, M. Broadband Terahertz Refraction Index Dispersion and Loss of Polymeric Dielectric Substrate and Packaging Materials. *J. Infrared Milli Terahz Waves* **2018**, *39* (1), 93−104.